International Journal of Nanoelectronics and Materials
IJNeaM
ISSN 1985-5761 | E-ISSN 2232-1535

Comparative analysis of the efficacy of bulk and membrane nanoporous materials in biological sensing

Shahidah Arina Shamsuddin [a,b] *, Adilah Ayoib [b,c], M. N. A. Uda [a,b], Jasni Ismail [b], N. A. Parmin [b], N. A. Karim [a,b], and M. N. Afnan Uda [d]

[a]*Faculty of Mechanical Engineering & Technology, Universiti Malaysia Perlis (UniMAP), 02600, Arau, Perlis, Malaysia*
[b]*Institute of Nano Electronic Engineering, Universiti Malaysia Perlis (UniMAP), Seriab, 01000 Kangar, Perlis, Malaysia*
[c]*Faculty of Chemical Engineering & Technology, Universiti Malaysia Perlis (UniMAP), 02100, Padang Besar, Perlis, Malaysia*
[d]*Faculty of Engineering, Universiti Malaysia Sabah, 88400 Kota Kinabalu, Sabah, Malaysia*
∗*Corresponding author. E-mail: shahidaharina@unimap.edu.my*

Received 22 September 2023, Revised 19 July 2024, Accepted 28 August 2024

ABSTRACT

Nanoporous materials possess significant potential in biological sensing applications due to their unique pore structures and high surface-area-to-volume ratios. Two common types of nanoporous materials are bulk and membrane-based. The differences in the structural and dimensional properties of nanopores are expected to impact the efficiency of biomolecule interactions during immobilization and hybridization, thereby influencing the overall performance of biological sensors. This study aims to investigate which type of nanoporous material offers enhanced sensitivity in detecting DNA targets. In this context, activated rice husk carbon (ARHC) and anodic aluminum oxide (AAO) were used to represent bulk and membrane nanoporous materials, respectively. Chitosan was mixed with ARHC to improve conductivity and provide better adhesion to the electrode substrate. ARHC and AAO thin films were characterized using SEM, XRD, and FTIR. Their performance in biological sensing was evaluated using Electrochemical Impedance Spectroscopy (EIS). Compared to chitosan/ARHC, the charge transfer resistance (R_{ct}) at the AAO/electrolyte interfaces was three times higher due to the smaller pore size and narrow, long nanoporous tunnel structure. Consequently, the sensitivity of the AAO thin film electrode in detecting DNA hybridization was lower (0.1312 $\Omega \cdot M^{-1}$) compared to the chitosan/ARHC electrode (0.0343 $\Omega \cdot M^{-1}$), which has a larger pore size and interconnected nanopore structures. The limit of detection (LOD) was also affected, with the AAO thin film electrode exhibiting a higher LOD of 3.0×10^{-13} M, while the chitosan/ARHC electrode demonstrated a lower and better LOD of 8.0×10^{-25} M. This study demonstrates that the type of nanoporous material significantly impacts sensitivity performance in biological sensing.

Keywords: *Bulk and membrane nanoporous, Activated carbon, AAO, DNA biosensor, FTIR, Electrochemical impedance spectroscopy*

1. INTRODUCTION

Materials with a large surface area to volume ratio are essential in biological sensing applications as they enable high load capacity, allowing for increased interactions between target biomolecules and sensing surfaces. Nanoporous materials are particularly suitable for such applications due to their large surface area-to-volume ratio [1]. In addition to their high loading capacity, nanoporous materials such as silicon nanopores [2, 3], anodic aluminum oxide (AAO) [4-6], zeolites [7-9], nanoporous gold [10, 11], and activated carbon [12-16] have been widely used as core materials in biosensor development. This widespread use is attributed to their unique characteristics, including biocompatibility, the ability to control pore shape, size, and design, as well as the flexibility to engineer their surfaces with specific bio-recognition elements such as antibodies, enzymes, or single-stranded DNA (ssDNA) during the immobilization process.

Nanoporous materials can be categorized into two main types based on their pore network structures, which are bulk and membrane nanoporous structures. Membrane nanoporous materials are typically produced using electrochemical anodization (e.g., for AAO and silicon nanopores) [17-20]. In contrast, bulk nanoporous materials are usually fabricated through track-etching techniques or dealloying (e.g., for gold nanoporous) [21, 22] or thermal carbonization/activation (e.g., for activated carbon) [23, 24]. Bulk nanoporous materials possess a continuous 3D interconnected pore network that allows unlimited access throughout the material, while membrane nanoporous materials have a 2D structure with a thin porous membrane layer on the surface, where the underlying material may be non-porous, thus providing only one-way access [25].

In this study, activated rice husk carbon (ARHC) was selected as the bulk nanoporous material, and anodic aluminum oxide (AAO) was selected as the membrane nanoporous material. The effectiveness of ARHC and AAO thin films in biological sensing applications may be influenced by their pore size and varied 2D/3D nanoporous structures. To investigate this, charge transfer resistance (R_{ct}) at the solid/electrolyte interfaces will be measured. ARHC will be combined with chitosan to form a conductive polymer matrix composite, with the aim of ensuring good

adhesion to the electrode substrate surfaces while improving conductivity. The sensitivity performance of chitosan/ARHC in detecting DNA hybridization will then be compared with that of the AAO thin film electrode.

2. MATERIALS AND METHODS

2.1. Synthesizing Bulk Nanoporous Activated Rice Husk Carbon (ARHC)

Raw rice husks were purchased from IRIZ GLOBAL MARKETING, Ayer Itam, Kedah, Malaysia. After being washed, cleaned, and dried, the raw rice husks were cut, blended, and sieved. Only rice husks ranging in size from 2 to 3 mm were selected for this study. The raw rice husks were carbonized in a tube furnace at 500°C to remove small organic molecules for 1 hour under nitrogen flow. Sodium hydroxide (NaOH) from Sigma Aldrich was used as the activating agent to synthesize bulk nanoporous-activated rice husk carbon (ARHC). The carbonized rice husks were mixed with NaOH in a 1:4 mass ratio (by weight), and the mixture was heated in a tube furnace at 500°C for 1 hour under nitrogen gas flow. The temperature was then raised to 800°C (with a heating rate of 10°C/min) and maintained for another hour to activate the carbon. Subsequently, the temperature was gradually decreased to room temperature. The ARHC was repeatedly rinsed with a 0.1 M hydrochloric acid solution and deionized water to neutralize it. After reaching a pH of 6.6-7.0, the ARHC was dried overnight in a vacuum oven at 120°C.

2.2. Synthesizing Membrane Nanoporous Anodic Aluminium Oxide (AAO)

For the preparation of aluminum (Al) thin film electrodes, a silicon oxide thin film layer was first grown on a cleaned 4-inch p-type silicon wafer (by New Wave Technology) using a wet oxidation process at 1000°C for 1 hour in an oxidation furnace as prior preparation for Al thin film deposition. A 99.99% pure Al wire (by Merck) was then deposited onto the silicon oxide surface to form an Al thin film layer via physical vapor deposition (PVD). The deposited Al thin film was subsequently annealed for 3 hours at 400°C in a muffle furnace and allowed to cool gradually to ambient temperature overnight to remove any stress that had accumulated during deposition, thus preventing the Al thin film from peeling off during anodization. Al thin film electrodes were prepared by cutting the Al/SiO_2 thin film wafer into 2 cm × 1 cm sizes. Insulating tape was applied to cover all the electrode surfaces except for the sensing and contact pad regions, as shown in Figure 1.

To synthesize anodic aluminum oxide (AAO) thin films, the anodization process was conducted as set up in Figure 1, by connecting the Al thin film electrode to the anode and a platinum electrode to the cathode. Both electrodes were immersed in 0.3 M oxalic acid (by Fisher Scientific) at 15°C for 1 hour at 40 V. An ice water bath technique was used to control and maintain the oxalic acid temperature at 15°C.

After 1 hour, the AAO thin film was rinsed with DI water and dried. A 20 µL drop of 5% (v/v) phosphoric acid solution (by Fisher Scientific) was then applied to the sensing region for 10 minutes to exfoliate the rough, uneven, and irregular pore surfaces, revealing and enlarging the underlying membrane nanopores. This procedure, known as etching, also introduced hydroxyl groups from the phosphoric acid onto the AAO membrane nanopores. After rinsing with DI water and drying, the AAO thin film electrodes were stored in closed containers at room temperature for further use.

2.3. Surface Chemical Functionalization of ARHC and AAO for DNA Complementation Preparation

Functionalization of ARHC and AAO nanoporous surfaces is necessary for their application as biological sensors. A 2% chitosan solution in 0.1 M acetic acid (Sigma Aldrich) was prepared for this purpose. The chitosan solution was mixed with ARHC in a centrifuge tube and sonicated for 20 minutes until a homogeneous mixture was obtained. Chitosan was added to ARHC to create a strong composite material with good adhesion to the substrate surface and improved conductivity. A 20 µL aliquot of the ARHC/chitosan mixture was dropped onto a cleaned bare Al thin film electrode substrate and allowed to dry at 30°C using a hotplate. To activate the carboxylic groups on the ARHC/chitosan surfaces, 20 µL of ethylene dichloride (EDC)/N-hydroxysuccinimide (NHS) (1:2 v/v ratio) solution in 0.1 M phosphate-buffered saline (PBS) (from Fisher Scientific and Sigma Aldrich) was applied to the ARHC/chitosan surfaces and incubated at 4°C for 5 hours. After incubation, the ARHC/chitosan electrode was rinsed with PBS solution and dried by blowing air. To immobilize the ssDNA probe, 10 µL of 10 µM aminated-ssDNA was applied to the ARHC/chitosan surfaces and incubated for 2 hours at room temperature. The unbound ssDNA probe was then removed from the ARHC/chitosan surfaces by rinsing them with PBS solution and drying them. For hybridization, 10 µL of 1 pM DNA target was applied to the ssDNA/ARHC/chitosan surfaces and incubated for 1 hour. The unbound DNA target

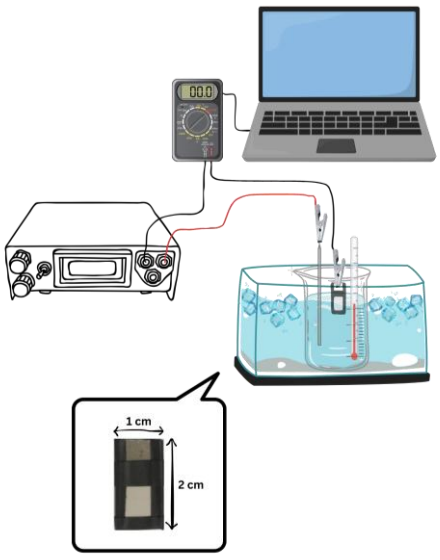

Figure 1. Anodization process setup for synthesizing AAO in 0.3 M of oxalic acid at 15°C for 1 hour at 40 V

was then removed by rinsing the ssDNA/ARHC/chitosan electrode with PBS solution and drying the user with a blower. This procedure was repeated with different concentrations ranging from 1 pM to 1 nM in ascending order.

Simultaneously, to functionalize the AAO membrane nanoporous surfaces, a 2% solution of 3-aminopropyl-triethoxysilane (APTES) (Sigma Aldrich) was applied to the AAO thin film electrode and incubated for 2 hours at room temperature. The AAO thin film was then rinsed with ethanol (Bendosen) to remove the excess APTES and dried using a blower. Next, a 2.5% solution of glutaraldehyde (GA) (Bendosen) was applied to the APTES/AAO surfaces and incubated for 1 hour. After rinsing off the excess glutaraldehyde with PBS solution and drying, 10 µL of 10 µM aminated-ssDNA probe was applied to the GA/APTES/AAO surface and incubated for 2 hours at room temperature. The remaining unbound ssDNA probes were removed by rinsing the AAO surface with PBS solution and drying. Subsequently, 10 µL of 10 fM DNA target was applied to the ssDNA/GA/APTES/AAO surfaces and incubated for 1 hour. The excess unbound DNA target was removed by rinsing it with a PBS solution and drying it. This procedure was repeated with different concentrations ranging from 10 fM to 10 µM. The DNA sequence of the coagulation factor VII (FVII) gene R353Q polymorphism was used in this study. First Base, Malaysia, synthesized all oligonucleotides. The sequence of the ssDNA probe is 5'-5AmM C6/CCA CTA CCA GGG CAC GT-3', and the DNA complementary target sequence is 5'-ACG TGC CCT GGT AGT GG-3'.

2.4. Characterization of Bulk ARHC and Membrane AAO Nanoporous

Scanning electron microscopy (SEM; JEOL JSM-6460LA) was utilized to observe the morphological changes from carbonized rice husk to ARHC. Meanwhile, field effect scanning electron microscopy (FESEM; Hitachi S-4800) was employed to examine the morphological changes of the AAO thin film before and after etching with phosphoric acid. ImageJ software was used to measure the dimensions of the nanopores. To analyze crystallinity, X-ray diffraction (XRD) was performed using a Bruker d2 Phaser at room temperature over a 2θ range from 5° to 90°, where Cu Kα radiation with a wavelength of 0.15416 nm was used at 30 mA and 40 kV. The diffraction patterns were analyzed using High Score Plus Software. ARHC and AAO thin film surface functionalities were identified using Fourier Transform Infrared Spectroscopy (FTIR) (Perkin Elmer), with measurement wavelengths ranging from 400 cm^{-1} to 4000 cm^{-1}. Prior to testing, ARHC was prepared as KBr pellets (in a ratio of 1:100 per mg).

2.5. Impedimetric Measurement and Analysis

To evaluate the sensitivity and limit of detection (LOD) performance of ARHC and AAO thin films in detecting DNA hybridization, electrochemical impedance spectroscopy (EIS) measurements were conducted using an α-Novocontrol Dielectric Analyzer. AAO thin film, platinum (Pt), and Ag/AgCl were connected as the working, counter, and reference electrodes. The measurements were performed in a mixed solution of 5 mM potassium ferricyanide ($K_3[Fe(CN)_6]$) and 5 mM potassium ferrocyanide ($K_4[Fe(CN)_6]$) in 0.1 M potassium chloride (KCl) over a frequency range from 10 MHz to 1 Hz, with an AC voltage of 2.5 mV. All chemicals used in the measurements were purchased from HmbG Chemicals. The NOVA 2.2 software was employed to fit the Nyquist plot and generate the equivalent circuit. The resistance charge transfer (R_{ct}) values were obtained from the fitted Nyquist plots and plotted on a linear regression graph. Sensitivity was calculated from the slope, while the LOD was determined using 3-sigma based on the standard deviation from the regular residual values of the plotted linear regression graph.

3. RESULTS AND DISCUSSION

3.1. Morphological Analysis

Figure 2 presents a morphological comparison between ARHC before and after activation with NaOH, and AAO thin film before and after etching with phosphoric acid. The carbonized rice husk shown in Figure 2(a) clearly exhibits a nonporous structure, in contrast to the ARHC depicted in Figure 2(b). The ARHC displays bulk porosity with non-oriented and irregular pore sizes ranging from 0.2 µm to 2 µm. This observation underscores the efficacy of the activation process, which successfully converts carbonized rice husk into porous ARHC through NaOH treatment at high temperatures.

In comparison to the ARHC, observations of the AAO thin film surface after etching, as seen under FESEM at 100kx magnification (Figure 2(d)), revealed a more orderly and uniform nanoporous structure. The average pore diameter, interpore distance, and wall thickness were measured at 77.96 nm, 111.06 nm, and 19.92 nm, respectively. Although the AAO film before etching (Figure 2(c)) exhibited small and uneven pores, it is theorized that these irregularities are remnants of the initial pores formed during the second stage of the anodization process. These initial pores likely guide the anodization process, facilitating the continuous growth and elongation of the AAO nanoporous membrane tunnels by providing mechanical tension between the pore walls. This process ultimately results in a well-aligned hexagonal structure with high regularity in the AAO nanoporous membrane.

3.2. Crystallinity Analysis

X-ray diffraction (XRD) was employed to assess the crystallinity of specific elements following chemical treatments. As shown in Figure 3, peaks observed at 23.75° and 34.14° correspond to silicon oxide and silicon nitride compounds, respectively, typically found in rice husk. However, these peaks disappeared after the carbonization process, as depicted in Figure 3(b), indicating the successful removal of these components. The transition from an

amorphous to a crystalline structure is evident from Figures 3(a) to (c), illustrating the complete transformation from the amorphous carbon phase of raw rice husk to the crystalline carbon phase of ARHC. The XRD pattern in Figure 3(c) reveals four distinct peaks at angles of 10.81°, 16.67°, 22.76°, and 42.36°, corresponding to the lattice planes (111), (002), (120), and (100) of carbon, respectively. This indicates that the analyzed ARHC possesses a micro-crystalline structure. These results are consistent with the findings of Gao *et al.* (2015), who observed that the increased intensity of carbon diffraction peaks is attributed to the high temperature used during the activation process, which leads to the formation of crystalline carbons and results in sharper and wider diffraction peaks [26].

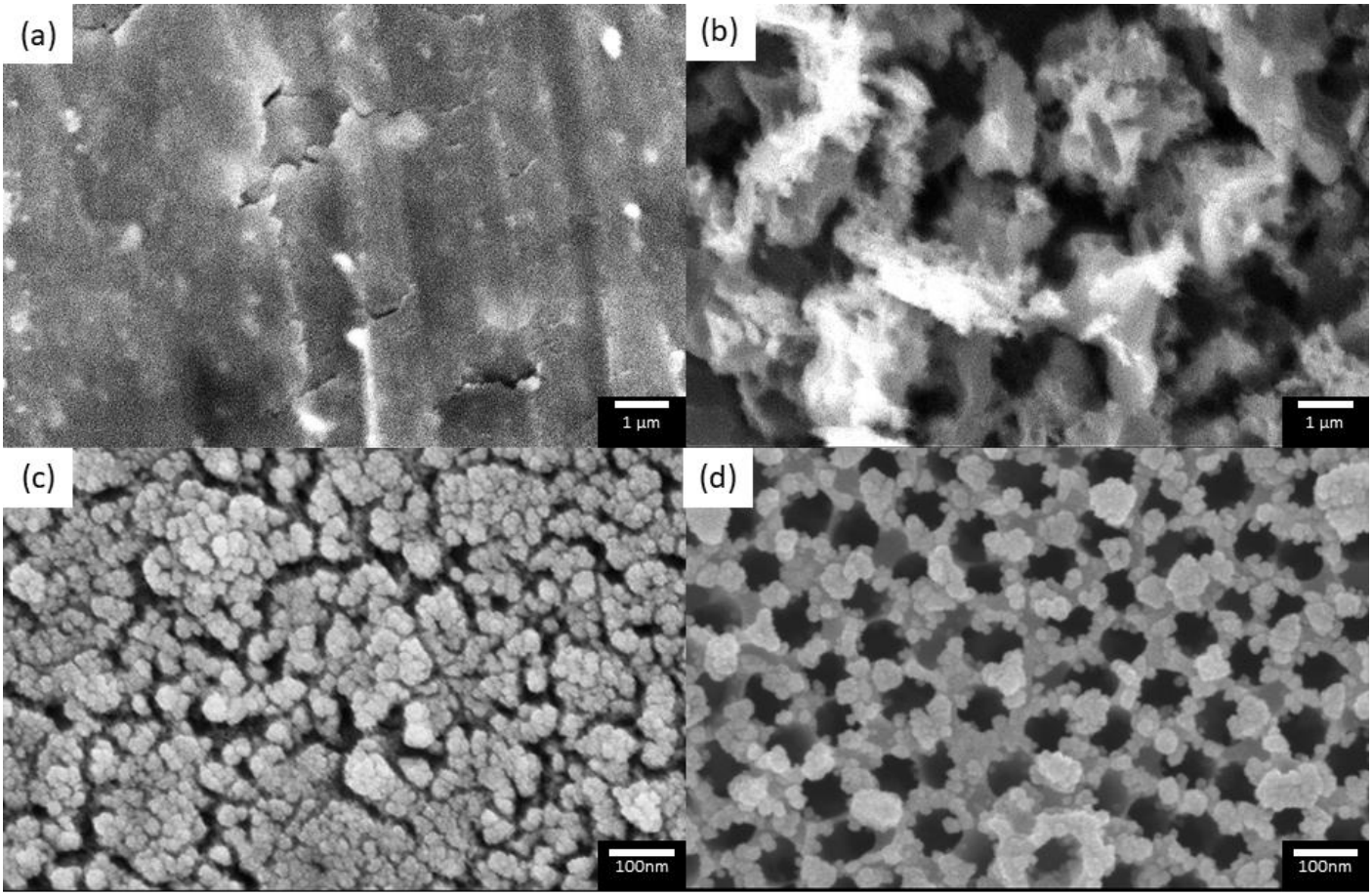

Figure 2. Morphological observation of ARHC at 10kx magnification (a) before and (b) after anodization, and AAO thin film at 100kx magnification (c) before and (d) after etching with phosphoric acid

XRD patterns of the AAO thin film are shown in Figure 4. The observed patterns reveal three distinct peaks at 38.56°, 44.56°, and 65.42°, which correspond to aluminum (Al) in a cubic face-centered structure (JCPDS: 04-0708) with lattice orientations (111), (200), and (220). Additionally, peaks at 29.54°, 39.58°, and 60.08° (JCPDS: 050-0741) correspond to cubic aluminum oxide, while peaks at 43.09°, 48.46°, and 69.25° (JCPDS: 01-070-3322) indicate a rhombohedral structure of aluminum oxide. The intensity of the aluminum oxide peaks is notably greater than that of the Al thin film, suggesting that a larger quantity of aluminum oxide was formed after anodization. Al metal undergoes oxidation at the anode during anodization, releasing three electrons and transforming into Al^{3+} cations. These cations then react with O^{2-} anions in the electrolytic solution, forming aluminum oxide. The decrease in the quantity of Al, as indicated by the reduced peak intensity of Al and the increased intensity of aluminum oxide peaks, is evident in Figure 4 [27, 28].

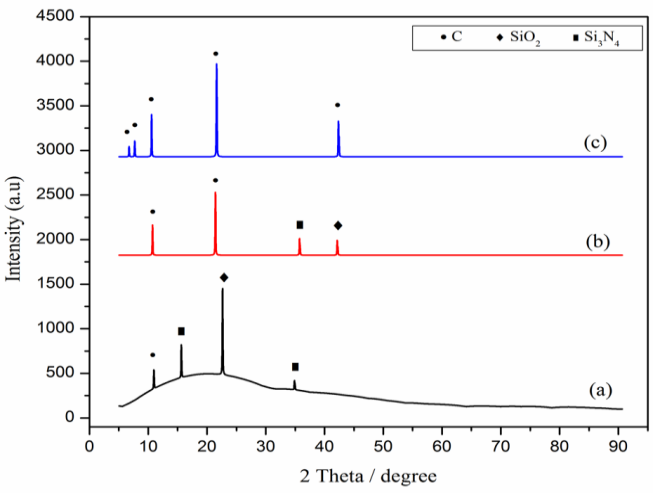

Figure 3. Diffraction peaks of (a) raw rice husk, (b) carbonized rice husk, and (c) ARHC

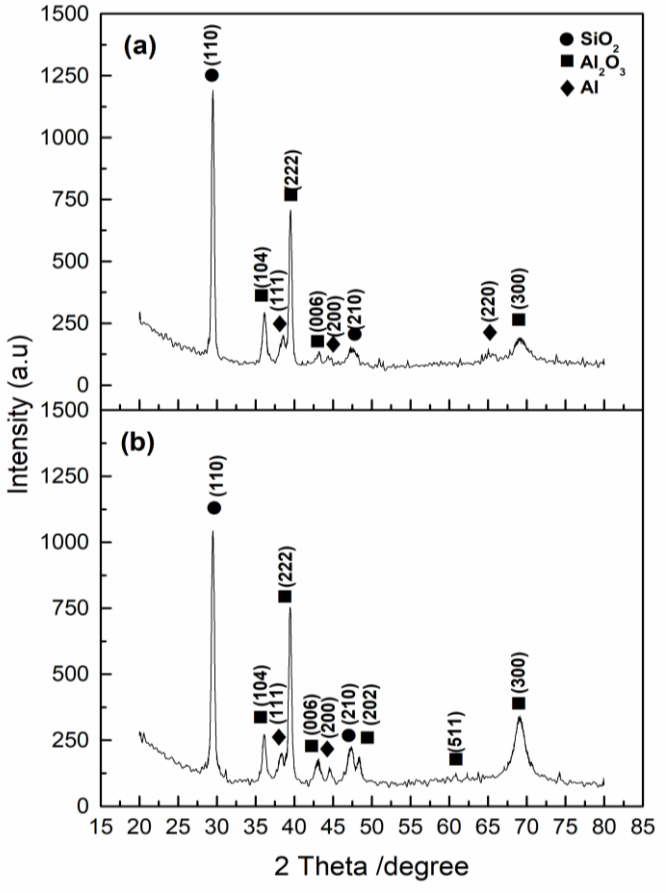

Figure 4. Diffraction peaks of (a) Al and (b) AAO thin films

Aluminum oxide can be classified into three distinct phases: α-phase, γ-phase, and amorphous alumina. The α-Al_2O_3 phase is naturally present in minerals such as corundum, ruby, sapphire, and emery. Conversely, γ-Al_2O_3 and amorphous phases are typically formed during anodization. Deposition of aluminum onto a substrate via either vacuum deposition or anodization results in a combination of amorphous alumina and γ-Al_2O_3 phases [27]. Therefore, the synthesized AAO is characterized as a mixture of amorphous alumina and γ-Al_2O_3. The XRD pattern in Figure 4 confirms this combination through high-intensity sharp peaks and smaller peaks for aluminum oxide. Additionally, the presence of silicon oxide (SiO_2) at 29.54° and 47.40° indicates tetragonal silicon oxide structures (JCPDS: 01-080-0369) with lattice orientations (110) and (210). Since silicon oxide was used as a substrate for AAO thin film electrodes, its appearance in the XRD patterns is expected.

3.3. Surface Chemical Analysis

The qualitative characterization of surface functional groups in ARHC samples was conducted using FTIR analysis. Figure 5 illustrates significant differences in the FTIR spectra among raw rice husk, carbonized rice husk, and ARHC. The surface functional groups of raw rice husk and carbonized rice husk are nearly identical, with only minor differences. The peak band in the range of 3500 cm^{-1} to 3000 cm^{-1} is assigned to the O-H stretching vibration of

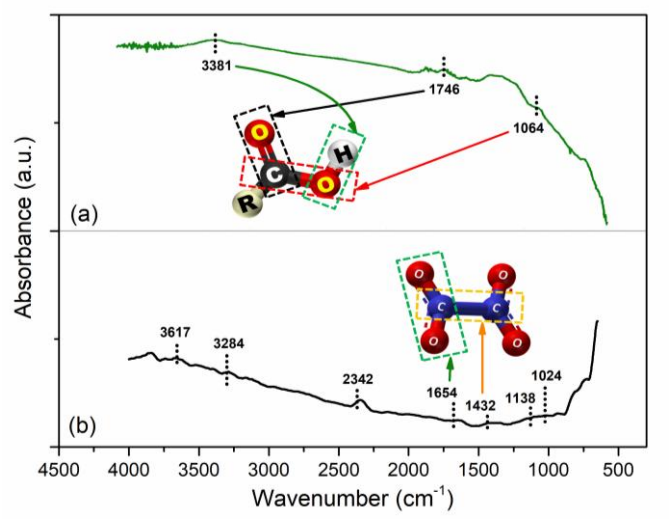

Figure 5. FTIR spectra of (a) ARHC and (b) AAO thin films

hydroxyl groups [29]. Bands at 1644 cm^{-1}, 1623 cm^{-1}, and 1579 cm^{-1} correspond to C=C stretching of aromatic rings, resulting from C-H deformation during the carbonization and activation process at temperatures between 500°C and 800C [30, 31]. The bands at 1169 cm^{-1}, 1092 cm^{-1}, and 1081 cm^{-1} are attributed to the C-O functional group in alcohols, phenols, ethers, or esters [29]. SiO_2 absorption peaks at 466 cm^{-1} are present in the FTIR spectra of raw and carbonized rice husk but disappear after the activation process, indicating the complete removal of silicon oxide by NaOH activation at elevated temperatures. This finding is corroborated by the XRD results, where peaks corresponding to silicon oxide and silicon nitride are absent after activation. Therefore, it can be concluded that ARHC is devoid of any silica content.

ARHC and AAO thin film surface functional groups were qualitatively characterized using FTIR absorbance analysis. Figure 5 demonstrates the differences in FTIR spectra between ARHC and AAO thin film. The spectral region between 3500 cm^{-1} and 3000 cm^{-1} corresponds to the stretching vibration of the O-H bond in hydroxyl groups [29]. Both ARHC and AAO thin films exhibit peaks in this region, indicating the presence of hydroxyl groups on their surfaces. During immobilisation, these hydroxyl groups are crucial for the subsequent modification of ARHC and AAO thin film with the aminated-ssDNA probe. To determine if the O-H stretch is associated with carboxylic groups (COOH), a peak in the range of 1650 cm^{-1} to 1750 cm^{-1} should be observed to represent the C=O bond stretch found in carboxylic acids. However, if the C=O peak appears alone without a distinct O-H stretch peak at 3500 cm^{-1} and 3000 cm^{-1}, the 1650 cm^{-1} to 1750 cm^{-1} peaks may indicate ketones, aldehydes, or esters. Additionally, the presence of a peak between 1000 cm^{-1} and 1300 cm^{-1} would be necessary to represent the C-C stretch bond. For ARHC, the presence of the O-H bond is accompanied by a C=O bond at 1746 cm^{-1}, indicating that the ARHC surface contains carboxylic groups, making it suitable for further activation by EDC and NHS to react with the aminated-ssDNA probe during immobilization chemically.

In contrast, the FTIR spectrum of the AAO thin film shows two important components. Figure 5 (b) reveals the presence of carboxylic acid (COOH) on the AAO thin film surface, evidenced by an O-H peak at 3284 cm^{-1} and a small C=O stretch peak at 1654 cm^{-1} [32]. However, the C=O stretch at 1654 cm^{-1} also corresponds to the symmetrical O-C-O bond from oxalate ions introduced during the anodization process. The additional peak at 1432 cm^{-1}, along with the peak at 1654 cm^{-1}, is attributed to the antisymmetric stretching vibration of C-C, supporting the presence of oxalate ions. During anodization, oxalate ions are thought to be attracted by the strong electric field at the bottom of the AAO nanoporous tunnels, moving toward the oxide/electrolyte interface and being incorporated into the growing barrier or oxide. Thus, oxalate ions can be detected near the AAO surfaces [5, 33-34]. Other peaks indicative of oxalate ions include those at 2342 cm^{-1} (C-O bond) and 1138 cm^{-1} (antisymmetric C-C stretching vibration). Finally, peaks around 1000 cm^{-1} or less are identified as complex vibrations of the Al-O bond [35, 36]. With the presence of COOH and C=O functionalities, the AAO thin film can be further modified with APTES in preparation for the immobilization of the ssDNA probe.

3.4. Sensitivity and Linear Regression Analysis

Sensitivity tests were conducted using EIS measurements across six different concentrations of complementary target DNA, ranging from 10 fM to 10 µM. Frequencies were applied from 10 MHz to 1 Hz at 2.5 mV. The equivalent circuit was determined by fitting the semicircle curves using NOVA 2.2. Figure 6 displays the equivalent circuit for both chitosan/ARHC and AAO thin film electrodes.

R_s refers to the solution resistance, while R_{ct} denotes the charge transfer resistance at the electrode's solid/electrolyte interfacial surfaces. The constant phase element (CPE), also known as the double layer capacitance, represents the porosity and roughness of the chitosan/ARHC and AAO thin film electrodes. CPE is more relevant than capacitance in describing ion transitions in these cases because the rough and nanoporous surfaces of the chitosan/ARHC and AAO thin film electrodes introduce nonhomogeneity, leading to variability in the relaxation times of electrolyte ions as they diffuse across the surfaces [37]. The impedimetric responses were plotted on Nyquist plots of Z imaginary (Z'') versus Z real (Z') for Faradaic impedance measurements of the chitosan/ARHC and AAO thin film electrodes, as shown in Figures 7 and 8, respectively.

The Nyquist plots indicate that the diameter of the semicircle curves increases with higher target concentrations. The semicircle in the middle-frequency region of the Nyquist plot represents the ion transport processes between the electrode surfaces and the current collector [30]. A smaller diameter of the semicircle corresponds to a lower impedance value, and vice versa. The R_{ct} values were obtained by fitting the Nyquist plot using NOVA 2.2. Table 1 presents the R_{ct} values of both electrodes at various target concentrations.

According to Table 1, the R_{ct} values exhibit an ascending trend with increasing DNA target concentrations. These trends are attributed to the rising number of successful dsDNA formations on the electrode surfaces after hybridization with DNA targets at higher concentrations. Additionally, it should be noted that dsDNA contains negatively charged phosphate groups in its structure.

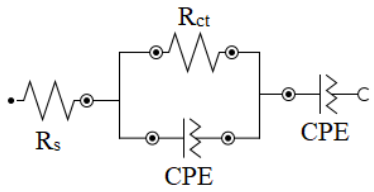

Figure 6. Equivalent circuit of Chitosan/ARHC and AAO thin film electrodes

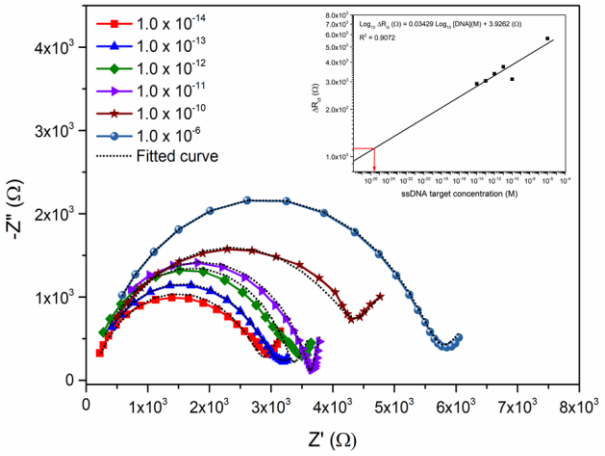

Figure 7. Nyquist plots of chitosan/ACRH electrodes in detecting hybridization of ssDNA target from 10 MHz to 1 Hz at 2.5 mV. The inset image is the linear regression graph of the chitosan/ACRH electrode sensitivity and LOD

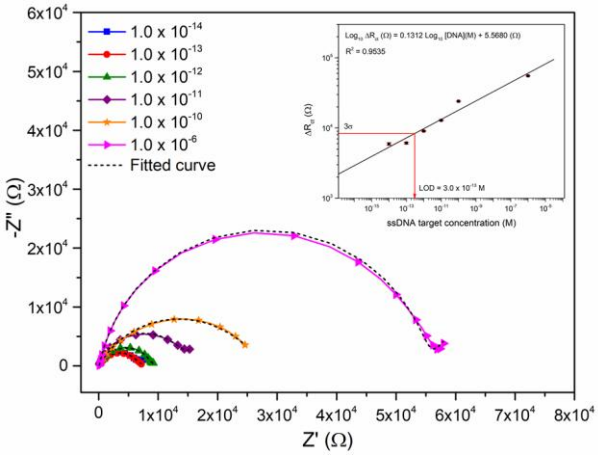

Figure 8. Nyquist plots of AAO thin film electrodes in detecting hybridization of ssDNA target from 10 MHz to 1 Hz at 2.5 mV. The inset image is the linear regression graph of the AAO thin film electrode sensitivity and LOD

Table 1. Charged transfer resistance (R_{ct}) values of Chitosan/ARHC and AAO thin film electrodes at different target concentrations

Target concentration (M)	Rct (Ω)	
	Chitosan/ARHC	AAO thin film
1.0×10^{-14}	2910	5923
1.0×10^{-13}	3041	6098
1.0×10^{-12}	3375	9023
1.0×10^{-11}	3736	12858
1.0×10^{-10}	3117	24071
1.0×10^{-6}	5660	55248

Simultaneously, the electrolyte ions used for measurement (ferrocyanide ions, $Fe(CN)_6^{3-}$) are also negatively charged. Consequently, the electrostatic repulsive forces between these two negatively charged entities cause some blockage in the diffusion of $Fe(CN)_6^{3-}$ ions to the solid/electrolyte interfaces, thereby affecting the current signal transfer. As a result, the R_{ct} increases with higher DNA target concentrations.

The sensitivity was calculated from the slope of the linear regression graph depicting ΔR_{ct} versus DNA target concentrations, as shown in the inset images in Figures 7 and 8. The sensitivities of the chitosan/ARHC and AAO thin films for detecting DNA hybridization are 0.0343 $\Omega.M^{-1}$ and 0.1312 $\Omega \cdot M^{-1}$, respectively. Additionally, based on the 3 sigma calculation, the limits of detection (LOD) are 8.0×10^{-25} M and 3.0×10^{-13} M, respectively. Clearly, the chitosan/ARHC electrode exhibits superior sensitivity and LOD compared to the AAO thin film electrode. The accuracy of the AAO thin film in detecting DNA targets at extremely low concentrations is questionable, as the lower limit of the linear range is 10 fM, which is lower than the calculated LOD of 300 fM. This suggests that while readings at very low target concentrations can still be detected, the signal may be very weak, non-linear, and affected by noise and interference.

The lower sensitivity and LOD performance of the AAO thin film electrode compared to the chitosan/ARHC can be explained by two factors. First, the increased conductivity achieved through the combination of chitosan and ARHC contributes to better electrical conductivity and sensitivity for detecting DNA hybridization compared to the AAO thin film. Second, the differences in nanopore size and structural type between the materials play a role. Morphological images reveal that the average pore size of ARHC is larger than that of the AAO nanopores. Additionally, the 2D versus 3D structure of the pores can affect electrode performance. The AAO thin film consists of a 2D structure, hexagonally aligned nanoporous membrane with elongated tunnels, whereas ARHC features a larger pore size and a 3D structure with unrestricted access. The smaller pore size and narrow tunnels of the AAO thin film may hinder the passage of biomolecules and measurement ions, exacerbating the resistance due to the electrostatic repulsion between DNA structures and $Fe(CN)_6^{3-}$ ions. Enhancing the sensitivity of the AAO thin film electrode could be achieved by enlarging the pore size, shortening the length of the 2D tunnels, or depositing highly conductive materials such as gold or titanium on the AAO thin film surface. Despite its limitations, however, the AAO thin film electrode demonstrates a better LOD compared to other reported optical biosensors, which have an LOD as low as 24 pM [38]. This result indicates that AAO label-free electrochemical sensors offer superior performance compared to optical-based sensors.

4. CONCLUSION

This study successfully developed chitosan/ARHC and AAO thin films for DNA hybridization detection. The sensitivity performance of both electrodes was compared, revealing that the chitosan/ARHC electrode outperforms the AAO thin film in detecting DNA hybridization. The smaller average diameter of the nanopores and the presence of long, narrow tunnels in the AAO thin film may impede the diffusion of biomolecules and measurement ions within the tunnels. In contrast, the larger diameter pores and the unrestricted access provided by the 3D structure of ARHC facilitate better ion movement. It can be concluded that the size of the nanopores and the 2D/3D structure of the pores significantly influence ion diffusion during measurements.

This research offers valuable insights into the electrochemical performance of 2D and 3D membrane nanoporous materials for biomolecule hybridization detection. It also suggests new avenues for research and identifies gaps for further improvement of these nanoporous structures as biosensor materials. Numerous variables and parameters warrant investigation to optimize and enhance the performance of both 2D and 3D nanoporous materials. Future research could focus on improving anodic aluminum oxide (AAO) as a biosensor electrode by incorporating gold nanoparticles or other conductive nanometallic materials to enhance AAO's conductivity. Additionally, optimization should aim at the pore diameter-to-the tunnel length ratio while at the same time, trying to reduce repulsive forces between biomolecules and electrode surfaces to lower charge transfer resistance and improve sensitivity.

ACKNOWLEDGMENTS

The author would like to acknowledge support from the Fundamental Research Grant Scheme (FRGS) under grant FRGS/1/2023/STG05/UNIMAP/02/9 from the Ministry of Higher Education Malaysia.

REFERENCES

[1] F. Izhar *et al.*, "Recent advances in metal-based nanoporous materials for sensing environmentally-related biomolecules," *Chemosphere*, vol. 307, p. 135999, Nov. 2022, doi: 10.1016/j.chemosphere. 2022.135999.

[2] G. A. Rodriguez, J. L. Lawrie, and S. M. Weiss, "Nanoporous silicon biosensors for DNA sensing," in *Porous Silicon for Biomedical Applications*, Elsevier, 2014, pp. 304–333. doi: 10.1533/9780857097156.2.

304.

[3] K. Awawdeh, M. A. Buttkewitz, J. Bahnemann, and E. Segal, "Enhancing the performance of porous silicon biosensors: the interplay of nanostructure design and microfluidic integration," *Microsystems & Nanoengineering*, vol. 10, no. 1, p. 100, Jul. 2024, doi: 10.1038/s41378-024-00738-w.

[4] J. Deng and C.-S. Toh, "Impedimetric DNA Biosensor Based on a Nanoporous Alumina Membrane for the Detection of the Specific Oligonucleotide Sequence of Dengue Virus," *Sensors*, vol. 13, no. 6, pp. 7774–7785, Jun. 2013, doi: 10.3390/s130607774.

[5] S. A. Shamsuddin, S. C. B. Gopinath, M. N. B. Derman, I. Jasni, C. Ibau, and M. F. M. Tahir, "Impedimetric transduction from a single-step thin film nanoporous aluminum oxide as a DNA sensing electrode," *Biochemical Engineering Journal*, vol. 202, p. 109149, Feb. 2024, doi: 10.1016/j.bej.2023.109149.

[6] S. Feng and W. Ji, "Advanced Nanoporous Anodic Alumina-Based Optical Sensors for Biomedical Applications," *Frontiers in Nanotechnology*, vol. 3, May 2021, doi: 10.3389/fnano.2021.678275.

[7] U. D. Kamaci, M. Kamaci, and A. Peksel, "Poly(azomethine-urethane) and zeolite-based composite: Fluorescent biosensor for DNA detection," *Spectrochimica Acta Part A: Molecular and Biomolecular Spectroscopy*, vol. 212, pp. 232–239, Apr. 2019, doi: 10.1016/j.saa.2019.01.011.

[8] R. Aguilar-Palma, M. Malankowska, and J. Coronas, "Applications of metal-organic frameworks and zeolites to virus detection and control: biosensors, barriers, and biocomposites," *Zeitschrift für anorganische und allgemeine Chemie*, vol. 647, no. 15, pp. 1532–1541, Aug. 2021, doi: 10.1002/zaac. 202000453.

[9] C. Chen, S. C. B. Gopinath, and P. Anbu, "Longitudinal Zeolite-Iron Oxide Nanocomposite Deposited Capacitance Biosensor for Interleukin-3 in Sepsis Detection," *Nanoscale Research Letters*, vol. 16, no. 1, p. 68, Dec. 2021, doi: 10.1186/s11671-021-03527-w.

[10] S. Xiao, S. Wang, X. Wang, and P. Xu, "Nanoporous gold: A review and potentials in biotechnological and biomedical applications," *Nano Select*, vol. 2, no. 8, pp. 1437–1458, Aug. 2021, doi: 10.1002/nano. 202000291.

[11] L. E. Ahangar and M. A. Mehrgardi, "Nanoporous gold electrode as a platform for the construction of an electrochemical DNA hybridization biosensor," *Biosensors and Bioelectronics*, vol. 38, no. 1, pp. 252–257, Oct. 2012, doi: 10.1016/j.bios.2012.05.040.

[12] R. Chen, H. Chen, H. Peng, Y. Zheng, Z. Lin, and X. Lin, "Multi-Walled Carbon Nanotube Array Modified Electrode with 3D Sensing Interface as Electrochemical DNA Biosensor for Multidrug-Resistant Gene Detection," *Biosensors*, vol. 13, no. 8, p. 764, Jul. 2023, doi: 10.3390/bios13080764.

[13] K. Hirayama *et al.*, "Attachment of DNA-Wrapped Single-Walled Carbon Nanotubes (SWNTs) for a Micron-Sized Biosensor," *ACS Omega*, vol. 7, no. 50, pp. 47148–47155, Dec. 2022, doi: 10.1021/ acsomega.2c06278.

[14] H. L. Poh, A. Bonanni, and M. Pumera, "Nanoporous carbon as a sensing platform for DNA detection: The use of impedance spectroscopy for hairpin-DNA based assay," *RSC Advances*, vol. 2, no. 3, pp. 1021–1024, 2012, doi: 10.1039/C1RA00812A.

[15] A. Khan, E. DeVoe, and S. Andreescu, "Carbon-based electrochemical biosensors as diagnostic platforms for connected decentralized healthcare," *Sensors & Diagnostics*, vol. 2, no. 3, pp. 529–558, 2023, doi: 10.1039/D2SD00226D.

[16] A. Kangmennaa, R. B. Forkuo, and E. S. Agorku, "Carbon-based electrode materials for sensor application: a review," *Sensing Technology*, vol. 2, no. 1, Dec. 2024, doi: 10.1080/28361466.2024.2350174.

[17] A. Santos, T. Kumeria, and D. Losic, "Nanoporous anodic aluminum oxide for chemical sensing and biosensors," *TrAC Trends in Analytical Chemistry*, vol. 44, pp. 25–38, Mar. 2013, doi: 10.1016/j.trac.2012. 11.007.

[18] C.-A. Ku, C.-Y. Yu, C.-W. Hung, and C.-K. Chung, "Advances in the Fabrication of Nanoporous Anodic Aluminum Oxide and Its Applications to Sensors: A Review," *Nanomaterials*, vol. 13, no. 21, p. 2853, Oct. 2023, doi: 10.3390/nano13212853.

[19] F. Rahimi, S. Fardindoost, F. Sepehri, F. Makiyan, A. Shafiekhani, and A. Hossein Rezayan, "Optimization of Porous Silicon Conditions for DNA-based Biosensing via Reflectometric Interference Spectroscopy," *Cell Journal (Yakhteh)*, vol. 20, no. 4, pp. 584–591, 2018, doi: 10.22074/cellj.2019.5598.

[20] M. B. de la Mora, M. Ocampo, R. Doti, J. E., and J. Faubert, "Porous Silicon Biosensors," in *State of the Art in Biosensors - General Aspects*, InTech, 2013. doi: 10.5772/52975.

[21] M. Yan *et al.*, "Ultrasensitive electrochemi-luminescence detection of DNA based on nanoporous gold electrode and PdCu@carbon nanocrystal composites as labels," *The Analyst*, vol. 137, no. 14, p. 3314, 2012, doi: 10.1039/c2an35267b.

[22] P. Daggumati, Z. Matharu, and E. Seker, "Effect of Nanoporous Gold Thin Film Morphology on Electrochemical DNA Sensing," *Analytical Chemistry*, vol. 87, no. 16, pp. 8149–8156, Aug. 2015, doi: 10.1021/acs.analchem.5b00846.

[23] J. Guo *et al.*, "Preparation and Characterization of Nanoporous Activated Carbon Derived from Prawn Shell and Its Application for Removal of Heavy Metal Ions," *Materials*, vol. 12, no. 2, p. 241, Jan. 2019, doi: 10.3390/ma12020241.

[24] S. Prasad Mishra, S. Dutta, A. Kumar Sahu, K. Mishra, and P. Kashyap, "Potential Application of Nanoporous Materials in Biomedical Field," in *Nanopores*, IntechOpen, 2021. doi: 10.5772/intechopen.95928.

[25] M. Hadden, D. Martinez-Martin, K.-T. Yong, Y. Ramaswamy, and G. Singh, "Recent Advancements in the Fabrication of Functional Nanoporous Materials and Their Biomedical Applications," *Materials*, vol. 15, no. 6, p. 2111, Mar. 2022, doi: 10.3390/ ma15062111.

[26] Y. Gao *et al.*, "Porous carbon made from rice husk as electrode material for electrochemical double layer capacitor," *Applied Energy*, vol. 153, pp. 41–47, Sep. 2015, doi: 10.1016/j.apenergy.2014.12.070.

[27] C. Lu and Z. Chen, "Anodic Aluminum Oxide–Based Nanostructures and Devices," *Encyclopedia of Nanoscience and Nanotechnology*, vol. 11. American Scientific Publishers, pp. 235–259, 2011.

[28] A. W. Juyana and M. N. B. Derman, "Characterization of Porous Anodic Aluminium Oxide Film on Aluminium Templates Formed in Anodizing Process," *Advanced Materials Research*, vol. 173, pp. 55–60, 2011, doi: 10.4028/www.scientific.net/AMR.173.55.

[29] A. R. Hidayu, N. F. Mohamad, S. Matali, and A. S. A. K. Sharifah, "Characterization of Activated Carbon Prepared from Oil Palm Empty Fruit Bunch Using BET and FT-IR Techniques," *Procedia Engineering*, vol. 68, pp. 379–384, 2013, doi: 10.1016/j.proeng.2013.12.195.

[30] H. D. Yoo, J. H. Jang, J. H. Ryu, Y. Park, and S. M. Oh, "Impedance analysis of porous carbon electrodes to predict rate capability of electric double-layer capacitors," *Journal of Power Sources*, vol. 267, pp. 411–420, Dec. 2014, doi: 10.1016/j.jpowsour.2014.05.058.

[31] R. Farma *et al.*, "Physical and Electrochemical Properties of Supercapacitor Electrodes Derived from Carbon Nanotube and Biomass Carbon," *International Journal of Electrochemical Science*, vol. 8, no. 1, pp. 257–273, Jan. 2013, doi: 10.1016/S1452-3981(23)14018-1.

[32] B. Smith, *Infrared Spectral Interpretation*. CRC Press, 2018. doi: 10.1201/9780203750841.

[33] K. Shimizu, H. Habazaki, P. Skeldon, G. E. Thompson, and G. C. Wood, "Migration of oxalate ions in anodic alumina," *Electrochimica Acta*, vol. 46, no. 28, pp. 4379–4382, Aug. 2001, doi: 10.1016/S0013-4686(01)00660-0.

[34] C. K. Chung, O. K. Khor, C. J. Syu, and S. W. Chen, "Effect of oxalic acid concentration on the magnetically enhanced capacitance and resistance of AAO humidity sensor," *Sensors and Actuators B: Chemical*, vol. 210, pp. 69–74, Apr. 2015, doi: 10.1016/j.snb.2014.12.096.

[35] I. Vida-Simiti, D. Nemes, N. Jumate, G. Thalmaier, and N. Sechel, "Self-Ordered Nanoporous Alumina Templates Formed by Anodization of Aluminum in Oxalic Acid," *JOM*, vol. 64, no. 10, pp. 1143–1147, Oct. 2012, doi: 10.1007/s11837-012-0406-1.

[36] M. E. Mata-Zamora and J. M. Saniger, "Thermal evolution of porous anodic aluminas: a comparative study," *Revista mexicana de física*, vol. 51, no. 5, pp. 502–209, 2005.

[37] V. Perumal *et al.*, "'Spotted Nanoflowers': Gold-seeded Zinc Oxide Nanohybrid for Selective Bio-capture," *Scientific Reports*, vol. 5, no. 1, p. 12231, Jul. 2015, doi: 10.1038/srep12231.

[38] X. Zhu, R. Wang, X. Zhou, and H. Shi, "Free-Energy-Driven Lock/Open Assembly-Based Optical DNA Sensor for Cancer-Related microRNA Detection with a Shortened Time-to-Result," *ACS Applied Materials & Interfaces*, vol. 9, no. 31, pp. 25789–25795, Aug. 2017, doi: 10.1021/acsami.7b06579.